letters to nature

Overall, this picture is in good agreement with direct theoretical predictions of the black-hole growth of SMGs and quasars[24,25].

What was the catalyst for the rapid black-hole and stellar growth seen in SMGs? Rest-frame ultraviolet images taken by the Hubble Space Telescope have shown that a considerably larger fraction of SMGs are in major mergers (that is, the merging of two galaxies of comparable masses) than has been found in the coeval galaxy population[17,27]. Hydrodynamical simulations have shown that major mergers can efficiently transport material towards the central regions of galaxies, providing an effective mechanism to trigger nuclear star formation and fuel the black hole[28]. The result of these major mergers is thought to be massive spheroid-dominated galaxies. Ultra-deep X-ray observations of SMGs undergoing major mergers have shown that AGN activity can be ongoing in both galactic components[12]. Presumably in these major-merger events the black holes will eventually coalesce, further increasing the mass of the black hole in the resultant galaxy. □

1. Tremaine, S. *et al.* The slope of the black hole mass versus velocity dispersion correlation. *Astrophys. J.* **574,** 740–753 (2002).
2. Yu, Q. & Tremaine, S. Observational constraints on the growth of massive black holes. *Mon. Not. R. Astron. Soc.* **335,** 965–976 (2002).
3. Barger, A. J. *et al.* The cosmic evolution of hard X-ray selected active galactic nuclei. *Astron. J.* **129,** 578–609 (2005).
4. McLure, R. J. & Dunlop, J. S. The cosmological evolution of quasar black hole masses. *Mon. Not. R. Astron. Soc.* **352,** 1390–1404 (2004).
5. Page, M. J., Stevens, J. A., Ivison, R. J. & Carrera, F. J. The evolutionary sequence of active galactic nuclei and galaxy formation revealed. *Astrophys. J.* **611,** L85–L88 (2004).
6. Smail, I., Ivison, R. J., Blain, A. W. & Kneib, J.-P. The nature of faint submillimetre-selected galaxies. *Mon. Not. R. Astron. Soc.* **331,** 495–520 (2002).
7. Chapman, S. C., Blain, A. W., Ivison, R. J. & Smail, I. R. A median redshift of 2.4 for galaxies bright at submillimetre wavelengths. *Nature* **422,** 695–698 (2003).
8. Hughes, D. H. *et al.* High-redshift star formation in the Hubble Deep Field revealed by a submillimetre-wavelength survey. *Nature* **394,** 241–247 (1998).
9. Chapman, S. C., Blain, A. W., Smail, I. R. & Ivison, R. J. A redshift survey of the submillimeter galaxy population. *Astrophys. J.* **622,** 2–26 (2005).
10. Stevens, J. A., Page, M. J., Ivison, R. J., Smail, I. & Carrera, F. J. A filamentary structure of massive star-forming galaxies associated with an X-ray-absorbed QSO at z = 1.8. *Astrophys. J.* **604,** L17–L20 (2004).
11. Croom, S. M. *et al.* The 2dF QSO Redshift Survey – XII. The spectroscopic catalogue and luminosity function. *Mon. Not. R. Astron. Soc.* **349,** 1397–1418 (2004).
12. Alexander, D. M. *et al.* The Chandra Deep Field North Survey. XIV. X-ray-detected obscured AGNs and starburst galaxies in the bright submillimeter source population. *Astron. J.* **125,** 383–397 (2003).
13. Ivison, R. J. *et al.* Spitzer observations of MAMBO galaxies: weeding out active nuclei in starbursting proto-ellipticals. *Astrophys. J. Suppl.* **154,** 124–129 (2004).
14. Greve, T. R. *et al.* An interferometric CO survey of luminous submm galaxies. *Mon. Not. R. Astron. Soc.* (in the press); preprint at ⟨http://arxiv.org/astro-ph/0503055⟩ (2005).
15. Tecza, M. *et al.* SPIFFI observations of the starburst SMM J14011+0252: Already old, fat, and rich by z = 2.565. *Astrophys. J.* **605,** L109–L112 (2004).
16. Swinbank, A. M. *et al.* The rest-frame optical spectra of SCUBA galaxies. *Astrophys. J.* **617,** 64–80 (2004).
17. Smail, I., Chapman, S. C., Blain, A. W. & Ivison, R. J. The rest-frame optical properties of SCUBA galaxies. *Astrophys. J.* **616,** 71–85 (2004).
18. Alexander, D. M. *et al.* The Chandra Deep Field North Survey. XIII. 2 Ms point-source catalogs. *Astron. J.* **126,** 539–574 (2003).
19. Alexander, D. M. *et al.* The X-ray properties of SCUBA galaxies. *Astrophys. J.* (submitted).
20. Veilleux, S., Kim, D.-C. & Sanders, D. B. Optical spectroscopy of the IRAS 1 Jy sample of ultraluminous infrared galaxies. *Astrophys. J.* **522,** 113–138 (1999).
21. Steidel, C. C. *et al.* A survey of star-forming galaxies in the 1.4 < z < 2.5 redshift desert: Overview. *Astrophys. J.* **604,** 534–550 (2004).
22. Fadda, D. *et al.* The AGN contribution to mid-infrared surveys. X-ray counterparts of the mid-IR sources in the Lockman Hole and HDF-N. *Astron. Astrophys.* **383,** 838–853 (2002).
23. Fabian, A. C. The obscured growth of massive black holes. *Mon. Not. R. Astron. Soc.* **308,** L39–L43 (1999).
24. Archibald, E. N. *et al.* Coupled spheroid and black hole formation, and the multifrequency detectability of active galactic nuclei and submillimetre sources. *Mon. Not. R. Astron. Soc.* **336,** 353–362 (2002).
25. Granato, G. L., De Zotti, G., Silva, L., Bressan, A. & Danese, L. A physical model for the coevolution of QSOs and their spheroidal hosts. *Astrophys. J.* **600,** 580–594 (2004).
26. Dunlop, J. S. *et al.* Quasars, their host galaxies and their central black holes. *Mon. Not. R. Astron. Soc.* **340,** 1095–1135 (2003).
27. Conselice, C. J., Chapman, S. C. & Windhorst, R. A. Evidence for a major merger origin of high-redshift submillimeter galaxies. *Astrophys. J.* **596,** L5–L8 (2003).
28. Springel, V., Di Matteo, T. & Hernquist, L. Black holes in galaxy mergers: the formation of red elliptical galaxies. *Astrophys. J.* **620,** L79–L82 (2005).
29. Elvis, M. *et al.* Atlas of quasar energy distributions. *Astrophys. J. Suppl.* **95,** 1–68 (1994).
30. Marconi, A. *et al.* Local supermassive black holes, relics of active galactic nuclei and the X-ray background. *Mon. Not. R. Astron. Soc.* **351,** 169–185 (2004).

....

Infrared radiation from an extrasolar planet

Drake Deming[1]**, Sara Seager**[3]**, L. Jeremy Richardson**[2]
& Joseph Harrington[4]

[1]*Planetary Systems Laboratory and Goddard Center for Astrobiology, Code 693;*
[2]*Exoplanet and Stellar Astrophysics Laboratory, Code 667, NASA's Goddard Space Flight Center, Greenbelt, Maryland 20771, USA*
[3]*Department of Terrestrial Magnetism, Carnegie Institution of Washington, 5241 Broad Branch Road NW, Washington DC 20015, USA*
[4]*Center for Radiophysics and Space Research, Cornell University, 326 Space Sciences Bldg, Ithaca, New York 14853-6801, USA*

A class of extrasolar giant planets—the so-called 'hot Jupiters' (ref. 1)—orbit within 0.05 AU of their primary stars (1 AU is the Sun–Earth distance). These planets should be hot and so emit detectable infrared radiation[2]. The planet HD 209458b (refs 3, 4) is an ideal candidate for the detection and characterization of this infrared light because it is eclipsed by the star. This planet has an anomalously large radius (1.35 times that of Jupiter[5]), which may be the result of ongoing tidal dissipation[6], but this explanation requires a non-zero orbital eccentricity (∼0.03; refs 6, 7), maintained by interaction with a hypothetical second planet. Here we report detection of infrared (24 μm) radiation from HD 209458b, by observing the decrement in flux during secondary eclipse, when the planet passes behind the star. The planet's 24-μm flux is $55 \pm 10 \mu Jy$ (1σ), with a brightness temperature of $1,130 \pm 150$ K, confirming the predicted heating by stellar irradiation[2,8]. The secondary eclipse occurs at the midpoint between transits of the planet in front of the star (to within ±7 min, 1σ), which means that a dynamically significant orbital eccentricity is unlikely.

Operating cryogenically in a thermally stable space environment, the Spitzer Space Telescope[9] has sufficient sensitivity to detect hot Jupiters at their predicted infrared flux levels[8]. We observed the secondary eclipse (hereafter referred to as 'the eclipse') of HD 209458b with the 24-μm channel of the Multiband Imaging Photometer for Spitzer (MIPS)[10]. Our photometric time series observations began on 6 December 2004 at 21:29 UTC (Coordinated Universal Time), and ended at approximately 03:23 UTC on 7 December 2004 (5 h 54 min duration). We analyse 1,696 of the 1,728 10-s exposures so acquired, rejecting 32 images having obvious flaws. The Supplementary Information contains a sample image, together with information on the noise properties of the data.

We first verify that circumstellar dust does not contribute significantly to the stellar flux. Summing each stellar image over a 13 × 13 pixel synthetic aperture (33 × 33 arcsec), we multiply the average sum by 1.15 to account for the far wings of the point spread function (PSF)[11], deriving a flux of 21.17 ± 0.11 mJy. The temperature of the star is close to 6,000 K (ref. 12). At a distance of 47 pc (ref. 13), a model atmosphere[14] predicts a flux of 22 mJy, agreeing

with our observed flux to within an estimated ∼2 mJy error in absolute calibration. We conclude that the observed flux is dominated by photospheric emission, in agreement with a large Spitzer study of planet-bearing stars at this wavelength[11].

Our time series analysis is optimized for high relative precision. We extract the intensity of the star from each image using optimal photometry with a spatial weighting function[15]. Selecting the Tiny Tim[16] synthetic MIPS PSF for a 5,000-K source at 24 µm, we spline-interpolate it to 0.01 pixel spacing, rebin it to the data resolution, and centre it on the stellar image. The best centring is judged by a least-squares fit to the star, fitting to within the noise level. The best-centred PSF becomes the weighting function in deriving the stellar photometric intensity. We subtract the average background over each image before applying the weights. MIPS data includes per-pixel error estimates[17], which we use in the optimal photometry and to compute errors for each photometric point. The optimal algorithm[15] predicts the signal-to-noise ratio (SNR) for each photometric point, and these average to 119. Our data are divided into 14 blocks, defined by pre-determined raster positions of the star on the detector. To check our SNR, we compute the internal

scatter within each block. This gives SNR in the range from 95 to 120 (averaging 111), in excellent agreement with the optimal algorithm. For each point we use the most conservative possible error: either the scatter within that block or the algorithm estimate, whichever is greater. We search for correlations between the photometric intensities and small fluctuations in stellar position, but find none. We also perform simple aperture photometry on the images, and this independent procedure confirms our results, but with 60% greater errors.

The performance of MIPS at 24 µm is known to be excellent[18]. Only one instrument quirk affects our photometry. The MIPS observing sequence obtains periodic bias images, which reset the detector. Images following resets have lower overall intensities (by ∼0.1–1%), which recover in later images. The change is common to all pixels in the detector, and we remove it by dividing the stellar intensities by the average zodiacal background in each image. We thereby remove variations in instrument/detector response, both known and unknown. The best available zodiacal model[19] predicts a background increase of 0.18% during the ∼6 h of our photometry. Because the star will not share this increase, we remove a 0.18% linear baseline from the stellar photometry. Note that the eclipse involves both a decrease and increase in flux, and its detection is insensitive to monotonic linear baseline effects.

To detect weak signals reliably requires investigating the nature of the errors. We find that shot noise in the zodiacal background is the dominant source of error; systematic effects are undetectable after normalizing any individual pixel to the total zodiacal background. All of our results are based on analysis of the 1,696 individual photometric measurements versus heliocentric phase from a recent
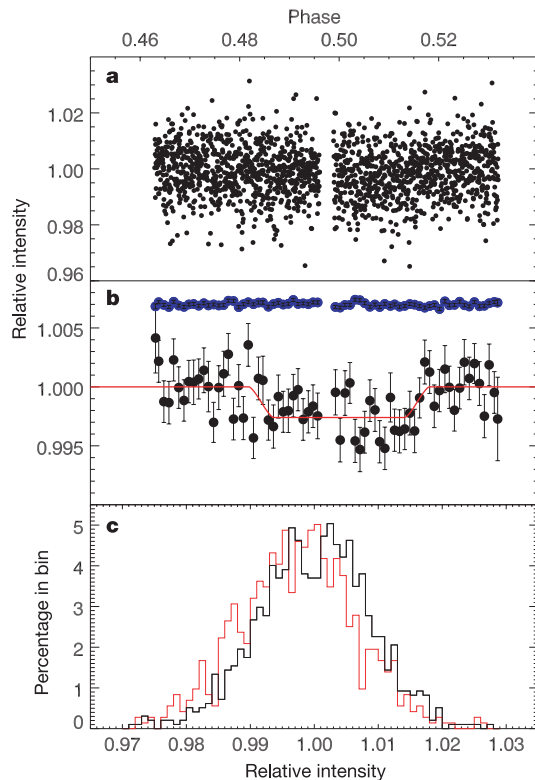

Figure 1 Observations showing our detection of the secondary eclipse in HD 209458. **a**, Relative intensities versus heliocentric phase (scale at top) for all 1,696 data points. The phase is corrected for light travel time at the orbital position of the telescope. Error bars are suppressed for clarity. The gap in the data near phase 0.497 is due to a pause for telescope overhead activity. The secondary eclipse is present, but is a factor of ∼4 below the ∼1% noise level of a single measurement. **b**, Intensities from **a**, averaged in bins of phase width 0.001 (scale at top), with 1σ error bars computed by statistical combination from the errors of individual points. The red line is the best-fit secondary eclipse curve (depth = 0.26%), constrained to a central phase of 0.5. The points in blue are a control sequence, summing intensities over a 10 × 10-pixel region of the detector, to beat down the random errors and reveal any possible systematic effects. The control sequence uses the same detector pixels, on average, as those where the star resides, but is sampled out of phase with the variations in the star's raster motion during the MIPS photometry cycle. **c**, Histograms of intensity (lower abscissa scale) for the points in **a**, with bin width 0.1%, shown separately for the out-of-eclipse (black) and in-eclipse intervals (red).
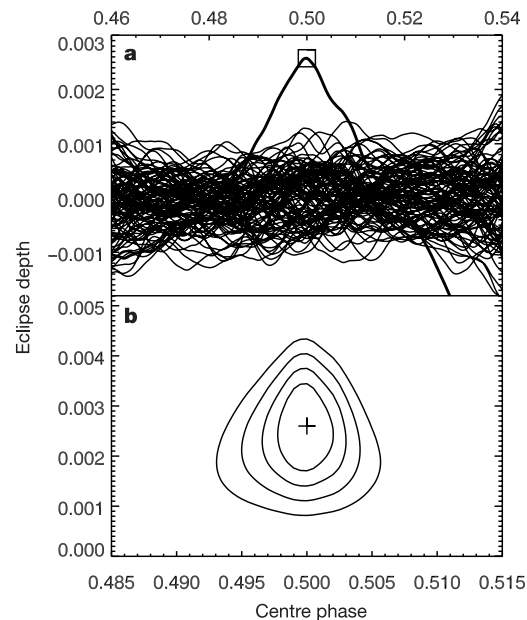

Figure 2 Amplitude of the secondary eclipse versus assumed central phase, with confidence intervals for both. **a**, The darkest line shows the amplitude of the best-fit eclipse curve versus the assumed central phase (scale at top). The overplotted point marks the fit having smallest χ^2, which also has the greatest eclipse amplitude. The numerous thinner black lines show the effect of fitting to 100 synthetic data sets containing no eclipse, but having the same per-point errors as the real data. Their fluctuations in retrieved amplitude versus phase are indicative of the error in eclipse amplitude, and are consistent with σ = 0.046%. Note that the eclipse amplitude found in the real data (0.26%) stands well above the error envelope at phase 0.5. **b**, Confidence intervals at the 1, 2, 3 and 4σ levels for the eclipse amplitude and central phase (note expansion of phase scale, at bottom). The plotted point marks the best fit (minimum χ^2) with eclipse depth of 0.26%, and central phase indistinguishable from 0.5. The centre of the eclipse occurs in our data at Julian day 2453346.5278.

ephemeris[20] (Fig. 1a). We propagate the individual errors (not shown on Fig. 1a) through a transit curve fit to calculate the error on the eclipse depth. Because about half of the 1,696 points are out of eclipse, and half are in eclipse, and the SNR $\approx$ 111 per point, the error on the eclipse depth should be $\sim 0.009 \times 2^{0.5}/848^{0.5} = 0.044\%$ of the stellar continuum. Model atmospheres for hot Jupiters[2,8,21–24] predict eclipse depths in the range from 0.2–0.4% of the stellar continuum, so we anticipate a detection of 4–9σ significance. The eclipse is difficult to discern by eye on Fig. 1a, because the observed depth (0.26%) is a factor of 4 below the scatter of individual points. We use the known period (3.524 days) and radii[5] to fit an eclipse curve to the Fig. 1a data, varying only the eclipse depth, and constraining the central phase to 0.5. This fit detects the eclipse at a depth of 0.26% $\pm$ 0.046%, with a reduced χ^2 of 0.963, denoting a good fit. Note that the 5.6σ significance applies to the aggregate result, not to individual points. The eclipse is more readily seen by eye on Fig. 1b, which presents binned data and the best-fit eclipse curve. The data are divided into many bins, so the aggregate 5.6σ significance is much less for a single bin (SNR $\approx$ 1 per point). Nevertheless, the dip in flux due to the eclipse is apparent, and the observed duration is approximately as expected. As a check, we use a control photometric sequence (Fig. 1b) to eliminate false positive detection of the eclipse due to instrument effects. We also plot the distribution of points in intensity for both the in-eclipse and out-of-eclipse phase intervals (Fig. 1c). This shows that the entire distribution shifts as expected with the eclipse, providing additional discrimination against a false positive detection.

We further illustrate the reality of the eclipse on Fig. 2. Now shifting the eclipse curve in phase, we find the best-fitting amplitude and χ^2 at each shift. This determines the best-fit central phase for the eclipse, and also further illustrates the statistical significance of the result. The thick line in Fig. 2a shows that the maximum amplitude (0.26%) is obtained at exactly phase 0.5 (which is also the minimum of χ^2). Further, we plot the eclipse 'amplitude' versus central phase using 100 sets of synthetic data, consisting of gaussian noise with dispersion matching the real data, but without an eclipse. The amplitude (0.26%) of the eclipse in the real data stands well above
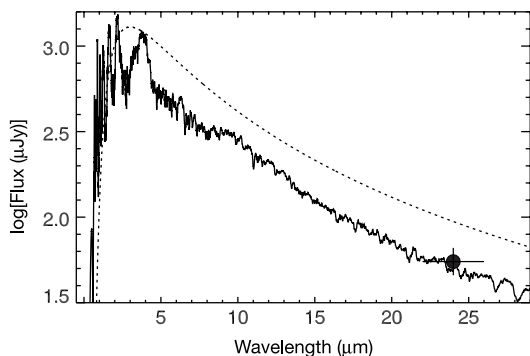
the statistical fluctuations in the synthetic data.

Figure 2b shows confidence intervals on the amplitude and central phase, based on the χ^2 values. The phase shift of the eclipse is quite sensitive to eccentricity (e) and is given[25] as $\Delta t = 2Pe\cos(\omega)/\pi$, where P is the orbital period, and ω is the longitude of periastron. The Doppler data alone give $e = 0.027 \pm 0.015$ (Laughlin, G., personal communication), and allow a phase shift as large as ± 0.017 (87 min). We find the eclipse centred at phase 0.5, and we checked the precision using a bootstrap Monte Carlo procedure[26]. The 1σ phase error from this method is 0.0015 (~ 7 min), consistent with Fig. 2b. A dynamically significant eccentricity, $e \approx 0.03$ (refs 6, 7), constrained by our 3σ limit of $\Delta t < 21$ min, requires $|(\omega - \pi/2)| < 12$ degrees and is therefore only possible in the unlikely case that our viewing angle is closely parallel to the major axis of the orbit. A circular orbit rules out a promising explanation for the planet's anomalously large radius: tidal dissipation as an interior energy source to slow down planetary evolution and contraction[7]. Because the dynamical time for tidal decay to a circular orbit is short, this scenario posited the presence of a perturbing second planet in the system to continually force the eccentricity—a planet that is no longer necessary with a circular orbit for HD209458b.

The infrared flux from the planet follows directly from our measured stellar flux (21.2 mJy) and the eclipse depth (0.26%), giving $55 \pm 10\,\mu$Jy. The error is dominated by uncertainty in the eclipse depth. Using the planet's known radius[5] and distance[13], we obtain a brightness temperature $T_{24} = 1{,}130 \pm 150$ K, confirming heating by stellar irradiation[2]. Nevertheless, T_{24} could differ significantly from the temperature of the equivalent blackbody (T_{eq}), that is, one whose bolometric flux is the same as the planet. Without measurements at shorter wavelengths, a model atmosphere must be used to estimate T_{eq} from the 24-μm flux. One such model is shown in Fig. 3, having $T_{eq} = 1{,}700$ K. This temperature is much higher than T_{24} (1,130 K) due to strong, continuous H_2O vapour absorption at 24 μm. The bulk of the planetary thermal emission derives ultimately from re-radiated stellar irradiation, and is emitted at 1–4 μm, between H_2O bands. However, our 24-μm flux error admits a range of models, including some with a significantly lower T_{eq} (for example, but not limited to, models with reflective clouds or less H_2O vapour).

Shortly after submission of this Letter, we became aware of a similar detection for the TrES-1 transiting planet system[27] using Spitzer's Infrared Array Camera[28]. Together, these Spitzer results represent the first measurement of radiation from extrasolar planets. Additional Spitzer observations should rapidly narrow the range of acceptable models, and reveal the atmospheric structure, composition, and other characteristics of close-in extrasolar giant planets. $\square$

Figure 3 Flux from a model atmosphere shown in comparison to our measured infrared flux at 24 μm. A theoretical spectrum (solid line) shows that planetary emission (dominated by absorbed and re-radiated stellar radiation) should be very different from a blackbody. Hence, models are required to interpret the 24-μm flux measurement in terms of the planetary temperature. The model shown has $T_{eq} = 1{,}700$ K and was computed from a one-dimensional plane-parallel radiative transfer model, considering a solar system abundance of gases, no clouds, and the absorbed stellar radiation re-emitted on the day side only. Note the marked difference from a 1,700-K blackbody (dashed line), although the total flux integrated over the blackbody spectrum is equal to the total flux integrated over the model spectrum. (The peaks at short wavelength dominate the flux integral in the atmosphere model, note log scale in the ordinate.) The suppressed flux at 24 μm is due to water vapour opacity. This model lies at the hot end of the range of plausible models consistent with our measurement, but the error bars admit models with cooler T_{eq}.

1. Collier-Cameron, A. Extrasolar planets: what are hot Jupiters made of? *Astron. Geophys.* **43,** 421–425 (2002).
2. Seager, S. & Sasselov, D. D. Extrasolar giant planets under strong stellar irradiation. *Astrophys. J.* **502,** L157–L161 (1998).
3. Charbonneau, D., Brown, T. M., Latham, D. W. & Mayor, M. Detection of planetary transits across a sun-like star. *Astrophys. J.* **529,** L45–L48 (2000).
4. Henry, G. W., Marcy, G. W., Butler, R. P. & Vogt, S. S. A transiting "51 Peg-like" planet. *Astrophys. J.* **529,** L41–L44 (2000).
5. Brown, T. M., Charbonneau, D., Gilliland, R. L., Noyes, R. W. & Burrows, A. Hubble Space Telescope time-series photometry of the transiting planet of HD 209458. *Astrophys. J.* **552,** 699–709 (2001).
6. Bodenheimer, P., Lin, D. N. C. & Mardling, R. A. On the tidal inflation of short-period extrasolar planets. *Astrophys. J.* **548,** 466–472 (2001).
7. Laughlin, G. *et al.* A comparison of observationally determined radii with theoretical radius predictions for short-period transiting extrasolar planets. *Astrophys. J.* (in the press).
8. Burrows, A., Sudarsky, D. & Hubeny, I. in *The Search for Other Worlds: Proc. 14th Annu. Astrophys. Conf. in Maryland* (eds Holt, S. & Deming, D.) Vol. 713, 143–150 (American Institute of Physics, Melville, New York, 2003).
9. Werner, M. W. *et al.* The Spitzer Space Telescope mission. *Astrophys. J. Suppl.* **154,** 1–9 (2004).
10. Rieke, G. H. *et al.* The Multiband Imaging Photometer for Spitzer (MIPS). *Astrophys. J. Suppl.* **154,** 25–29 (2004).

11. Beichman, C. A. *et al.* Planets and IR excesses: preliminary results from a *Spitzer* MIPS survey of solar-type stars. *Astrophys. J.* (in the press).

12. Ribas, A. H., Solano, E., Masana, E. & Gimenez, A. Effective temperatures and radii of planet-hosting stars from IR photometry. *Astron. Astrophys.* **411**, L501–L504 (2003).

13. Perryman, M. A. C. (ed.) *The Hipparcos and Tycho Catalogues* (ESA SP-1200, European Space Agency, Noordwijk, 1997).

14. Kurucz, R. *Solar Abundance Model Atmospheres for 0, 1, 2, 4, and 8 km/s* CD-ROM 19 (Smithsonian Astrophysical Observatory, Cambridge, Massachusetts, 1994).

15. Horne, K. An optimal extraction algorithm for CCD spectrososcopy. *Publ. Astron. Soc. Pacif.* **98**, 609–617 (1986).

16. Krist, J. in *Astronomical Data Analysis Software and Systems IV* (eds Shaw, R. A., Payne, H. E. & Hayes, J. J. E.) Vol. 77, 349–352 (Astronomical Society of the Pacific, San Francisco, 1995).

17. Gordon, K. D. Reduction algorithms for the Multiband Imaging Photometer for SIRTF. *Publ. Astron. Soc. Pacif.* (in the press).

18. Rieke, G. H. *et al.* in *Proc. SPIE: Optical, Infrared, and Millimeter Space Telescopes* (ed. Mather, J. C.) Vol. 5487, 50–61 (SPIE, Bellingham, Washington, 2004).

19. Kelsall, T. *et al.* The COBE Diffuse Infrared Background Experiment (DIRBE) search for the cosmic infrared background. II. Model of the interplanetary dust cloud. *Astrophys. J.* **508**, 44–73 (1998).

20. Wittenmyer, R. A. *The Orbital Ephemeris of HD 209458b.* Master's thesis, San Diego State Univ. (2003).

21. Goukenleuque, C., Bezard, B., Joguet, B., Lellouch, E. & Freedman, R. A radiative equilibrium model of 51 Peg b. *Icarus* **143**, 308–323 (2000).

22. Seager, S., Whitney, B. A. & Sasselov, D. D. Photometric light curves and polarization of close-in extrasolar giant planets. *Astrophys. J.* **540**, 504–520 (2000).

23. Barman, T. S., Hauschildt, P. H. & Allard, F. Irradiated planets. *Astrophys. J.* **556**, 885–895 (2001).

24. Sudarsky, D., Burrows, A. & Hubeny, I. Theoretical spectra and atmospheres of extrasolar giant planets. *Astrophys. J.* **588**, 1121–1148 (2003).

25. Charbonneau, D. in *Scientific Frontiers in Research on Extrasolar Planets* (eds Deming, D. & Seager, S.) Vol. 294, 449–456 (Astronomical Society of the Pacific, San Francisco, 2003).

26. Press, W. H., Teukolsky, S. A., Vettering, W. T. & Flannery, B. P. *Numerical recipes in C* 2nd edn (Cambridge Univ. Press, Cambridge, 1992).

27. Alonso, R. *et al.* TrES-1, the transiting planet of a bright K0V star. *Astrophys. J.* **613**, L153–L156 (2004).

28. Charbonneau, D. *et al.* Detection of thermal emission from an extrasolar planet. *Astrophys. J.* (in the press).

- -

Tuning clathrate hydrates for hydrogen storage

Huen Lee[1], Jong-won Lee[1], Do Youn Kim[1], Jeasung Park[1], Yu-Taek Seo[2]*, Huang Zeng[2], Igor L. Moudrakovski[2], Christopher I. Ratcliffe[2] & John A. Ripmeester[2]

[1]*Department of Chemical and Biomolecular Engineering, Korea Advanced Institute of Science and Technology (KAIST), Daejeon 305-701, Republic of Korea*
[2]*Steacie Institute for Molecular Sciences, National Research Council Canada, Ottawa, Ontario, Canada K1A 0R6*

* Present address: Conversion Process Research Center, Korea Institute of Energy Research, PO Box 103, Jang-dong, Yuseong-gu, Daejeon 305-343, Republic of Korea

- -

The storage of large quantities of hydrogen at safe pressures[1] is a key factor in establishing a hydrogen-based economy. Previous strategies—where hydrogen has been bound chemically[2], adsorbed in materials with permanent void space[3] or stored in hybrid materials that combine these elements[3]—have problems arising from either technical considerations or materials cost[2–5]. A recently reported[6–8] clathrate hydrate of hydrogen exhibiting

two different-sized cages does seem to meet the necessary storage requirements; however, the extreme pressures ($\sim$2 kbar) required to produce the material make it impractical. The synthesis pressure can be decreased by filling the larger cavity with tetrahydrofuran (THF) to stabilize the material[9], but the potential storage capacity of the material is compromised with this approach. Here we report that hydrogen storage capacities in THF-containing binary-clathrate hydrates can be increased to $\sim$4 wt% at modest pressures by tuning their composition to allow the hydrogen guests to enter both the larger and the smaller cages, while retaining low-pressure stability. The tuning mechanism is quite general and convenient, using water-soluble hydrate promoters and various small gaseous guests.

The structure II (sII) hydrates constitute a large family of clathrates with an ideal unit cell $16S \cdot 8L \cdot 136H_2O$, where the large (L) and small (S) cavities can be filled with guest molecules[10]. The 'solid solution' theory of van der Waals and Platteeuw, the classical approach to understanding clathrate behaviour, uses the basic expression:

$$\Delta\mu_w = -kT\Sigma_i \nu_i \ln(1 - \Theta_i) \qquad (1)$$

which relates the free energy difference, $\Delta\mu_w$, between ice and a hypothetical empty hydrate framework to the minimum occupancy Θ_i of the hydrate cavities of type i required to render it stable; ν_i are the number of cages of type i in the unit cell normalized by the number of water molecules. For sII hydrate, the 'best value' of $\Delta\mu_w$ of 884 J mol^{-1} requires the large cages to be filled to more than 99% for stability. This is consistent with the observation that many sII hydrates are known for which the stoichiometry is $L \cdot 17H_2O$ within experimental error. The small cages can be occupied by a small guest, leading to a double hydrate, $(2S)_x \cdot L \cdot 17H_2O$, generally stable to higher temperatures, where x is the fractional occupancy of the small cages, as recently illustrated[9] for THF and H_2 ($x \approx 1$, 1 wt% H_2). The recently reported H_2 clathrate is also sII with multiple occupancy of the cages (4 in L, 2 in S)[6–8]. Double hydrates represent an opportunity to engineer hybrid structures that combine H_2 storage capacity with much less severe synthetic pressures.

We carried out initial studies on materials produced from 5.56 mol% THF solution in water, which gives a clathrate of composition $THF \cdot 17H_2O$ when cooled below the melting point of 277.3 K. The THF hydrate was then pressurized with H_2 gas at various pressures up to $\sim$120 bar, and examined for structure, cage populations and composition by powder X-ray diffraction (PXRD), Raman and NMR spectroscopy, and direct measurement of the H_2 released on decomposition. From the PXRD results (Supplementary Fig. 1 and Supplementary Table 1), the material was confirmed to be a sII hydrate according to its phase behaviour (Supplementary Fig. 2). The Raman spectra (Fig. 1) show four transitions due to rotational fine structure associated with the high-pressure H_2 gas, and a broad band that can be identified with H_2 inside hydrate cages. The hydrate H_2 line is shifted to lower frequency compared to the free gas[11], as has also been observed for O_2 and N_2 hydrates[12]. ^1H NMR spectroscopy was used to monitor H_2 in the product of the reaction of H_2 with perdeuterated THF hydrate (THF-d$_8 \cdot 17D_2O$), so that only H_2 signals and residual protons in water and THF would be observed. The spectra in Fig. 2 show a broad line at 4.3 p.p.m. that can be attributed to H_2 in the small cavities of the double hydrate. Full loading of the small cavities of $THF \cdot 17H_2O$ with hydrogen (2H_2 per small cage) will result in a storage capacity of 2.1 wt% H_2.

Is it possible to obtain higher hydrogen loading, while keeping the H_2 pressure at a reasonable value? Although double hydrates have been known for over a century, techniques for hydrate analysis in terms of guest distribution over the hydrate cage sites were developed only recently, so little effort has gone into attempts to tune hydrate compositions. In order to increase the hydrogen content of the hydrate, the hydrogen guest must also enter the